Article

# Universal bimodality in kinematic morphology and the divergent pathways to galaxy quenching

Bitao Wang [1,2] ✉, Yingjie Peng [1,2] ✉ & Michele Cappellari [3]

The hierarchical structure formation of our Universe inherently involves disruptive and chaotic episodes of mass assembly such as galaxy mergers. The level of bulk rotation of the collisionless stellar systems of galaxies reflects to what extent the galaxies, on the other hand, have assembled their stars during tranquil and ordered formation history, which fosters the growth of cohesively rotating structures. Observationally, galaxy populations show a wide spectrum of morphology and shapes, with different levels of rotational support. Despite the obvious variety and complexity, in this work we find that, at a given stellar mass of galaxies, the distribution of the intrinsic spin parameter $\lambda_{R_e,\text{intr}}$, that is, the normalized specific angular momentum of stars, appears to be universally bimodal among galaxies in all star-formation states and also in different environments. This ubiquitous bimodality in kinematic morphology evolves systematically with star formation and is particularly apparent for transitional galaxies of intermediate star-formation rates, which indicates that star-formation quenching is proceeding separately within two distinct kinematic populations dominated by cold disks and hot spheroids. We show that the two populations also have contrasting recent star-formation histories and metal-enrichment histories, which reveal their divergent pathways to formation and quenching.

Physical processes involving angular momentum transfer, such as galaxy mergers and disc instability, can alter stellar orbits and eventually lead to star ensembles of different morphology[1–4]. Modern surveys of integral field spectroscopy[5–9] provide spatially resolved kinematic maps for thousands of galaxies and have enabled statistical studies of angular momentum for galaxy populations across diverse environments. Previous works[10–15] have discussed how the galaxy-formation history might be related to the kinematic properties of these local populations. However, different conclusions have been drawn about whether the underlying distributions of various quantifications of galaxy rotational support can be considered bimodal, or whether there are more complex factors at play.

Taking a step further from our previous study[13], where we show that the stellar spin λ_{R_e}, on average, reduces with decreasing star-formation rate (SFR), here we explore the detailed distributions of λ_{R_e} at given stellar mass and SFR. The dots in the left panel of Fig. 1 show the galaxies studied in this work on the SFR versus stellar mass $\mathcal{M}_\star$ diagram. These ~3,000 local galaxies, covering a wide range in morphology and environment, have available maps of stellar mean velocity and velocity dispersion from the Mapping Nearby Galaxies at Apache Point Observatory survey[9] (MaNGA), as a part of Data Release 15 of The Sloan Digital Sky Survey[16] (SDSS). With quality control, λ_{R_e} is determined based on MaNGA kinematic maps[17], and the stellar mass and SFR are derived by fitting the spectral energy distribution (SED) from ultraviolet (UV) to infrared (IR) wavelength[18,19].

[1]Department of Astronomy, School of Physics, Peking University, Beijing, China. [2]Kavli Institute for Astronomy and Astrophysics, Peking University, Beijing, China. [3]Sub-department of Astrophysics, Department of Physics, University of Oxford, Oxford, UK. ✉e-mail: bt-wang@pku.edu.cn; yjpeng@pku.edu.cn
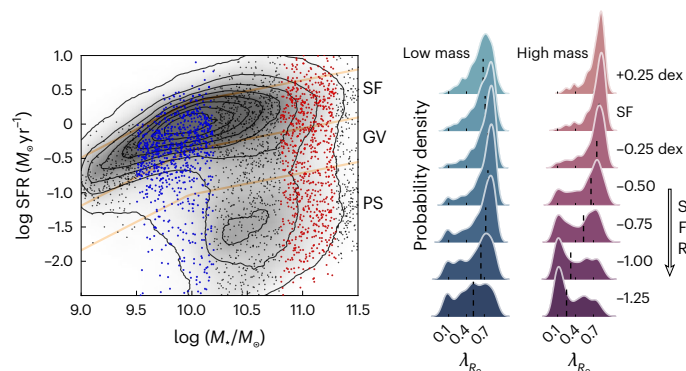
Fig. 1 | A highlight of the bimodal λ_{R_e} variation with SFR among massive galaxies. Left, the SFR versus stellar mass diagram for MaNGA galaxies (dots) and a much larger sample of galaxies from the main SDSS spectroscopic survey (shaded contours). The three yellow lines mark the loci +0.35, −0.35 and −1 dex from the SFMS, and the SFMS is determined by the ridge of the upper contour, as a benchmark of normal star formation. Throughout this work, galaxies are divided into three star-formation levels by the distance to the SFMS: SF, −0.35 < Δlog SFR < 0.35; GV, −1 < Δlog SFR < −0.35; and PS, Δlog SFR < −1. Among MaNGA galaxies, blue and red dots show the positions of those in representative low-mass and high-mass bins, respectively (blue: $10^{9.5} < \mathcal{M}_\star/\mathcal{M}_\odot < 10^{10.2}$; red: $10^{10.8} < \mathcal{M}_\star/\mathcal{M}_\odot < 10^{11.3}$). Right, two columns, coloured correspondingly, show the λ_{R_e} distribution as a function of SFR for MaNGA galaxies in the two representative mass bins, respectively. Each panel shows the kernel estimated density distribution and the median value (black dotted line) of λ_{R_e} of galaxies in a certain Δlog SFR window of width 0.7 dex. From top to bottom, the centre of the window goes from high to low star formation in steps of 0.25 dex, with the window centres relative to the SFMS denoted on the rightmost.

To quantify the star-formation state in the broad context of the local Universe, we use ~700,000 galaxies in the same redshift range and with consistent mass and SFR measurements, which are a major part of the Main Galaxy Sample[20] of the SDSS. The contours and grey shading illustrate the density distribution of these ~700,000 galaxies from which we define the ridge line (with volume correction) of the upper cloud of star-forming (SF) galaxies as the star-formation main sequence (SFMS)[21]. Galaxies around the SFMS are thought to be in dynamical equilibrium between gas inflow, star formation and gas outflow[22,23]. We define those with −0.35 < Δlog SFR < 0.35 from the SFMS (between the upper two yellow lines) as normal SF galaxies. Galaxies below the lowest yellow line, which have SFR less than 10% of SF galaxies on the SFMS (Δlog SFR < −1), are quiescent and passive (PS galaxies). Other galaxies with intermediate SFR (−1 < Δlog SFR < −0.35) are in the 'valley' of the density distribution. These galaxies generally also have intermediate colour index compared with SF and PS galaxies, and are commonly defined as green valley (GV) galaxies.

In the right-hand two columns of Fig. 1, we highlight how the normalized λ_{R_e} distribution varies with SFR among representative low- and high-mass galaxies (blue: $10^{9.5} < \mathcal{M}_\star/\mathcal{M}_\odot < 10^{10.2}$; red: $10^{10.8} < \mathcal{M}_\star/\mathcal{M}_\odot < 10^{11.3}$). From top to bottom, each panel shows the probability density distribution derived from Gaussian kernel estimation and the median (black dotted line) of λ_{R_e} for galaxies in sliding windows (0.7 dex wide and 0.25 dex step) of distance to the SFMS. The positions of the windows with respect to the SFMS are marked on the rightmost.

For high-mass galaxies, from the SFMS to lower star-formation levels, a twin peak at low λ_{R_e} gradually emerges whereas the high λ_{R_e} peak diminishes. The change of the median value of λ_{R_e} is hence primarily due to the variation in the relative importance of the two peaks, rather than the move or broadening of individual peaks in the distribution. Notably, the median or average value of λ_{R_e} is far from being a good representation of the bimodal distribution among massive GV galaxies. We have checked that this λ_{R_e} bimodality clearly exists even if we do not correct for atmospheric smearing and it is not due to any

bimodality in the distribution of SFR or mass. There is a hint of a similar separation among low-mass galaxies. However, the growing tail at low λ_{R_e} towards low star-formation levels contains only a small number of galaxies. Previous evidence suggests that many of them host counter-rotating disks[17] and are not genuine triaxial slow rotators like the massive systems. The nature of these seemingly slow-rotating, low-mass systems also bears uncertainty resulting from lower signal-to-noise ratio and spatial resolution compared with massive galaxies.

To remove the projection effect and determine the fractions of the underlying fast- and slow-rotating population, we build theoretical models and estimate the distributions of the intrinsic λ_{R_e} (that is, λ_{R_e} observed edge-on). The models we use are based on the tensor virial theorem that links together shape, ordered to random motion ratio and velocity anisotropy for axisymmetric galaxies[24]. The theoretical galaxy population constructed with the models are assumed to have an intrinsic ellipticity ε_{intr} distribution composed of two Gaussian components which stand for the fast- and slow-rotating population, respectively. The theoretical populations are then projected onto the sky plane at random orientation, giving a projected global stellar spin λ_R distribution to be compared with observations. A simplification is implied in the above modelling. The slow rotators of low intrinsic stellar spin $\lambda_{R_e,intr}$ in the real world have diverse shapes[10,25,26]. Although some of them are mildly triaxial[27] and some have not so small ellipticity due to the existence of counterrotating disks, here we treat them all as axisymmetric galaxies with single kinematic component, to enable them to be readily described by the tensor virial theorem. This simplification does not affect the conclusion, given our focus on the angular momentum of galaxies rather than their detailed shapes. We get consistent results if we just model galaxies excluding the classic slow rotators (defined by equation 19 of ref. 11) and integrate the observed λ_{R_e} distribution of classic slow rotators into the derived $\lambda_{R_e,intr}$ distributions of other galaxies.

The black solid lines in the upper half of the panels of Fig. 2 show the observed λ_{R_e} probability density distribution in four mass bins (denoted at the top) for SF, GV and PS galaxies, respectively. One hundred bootstrap samples are created and the inner 68% (in between 16% and 84% percentiles) of their density distributions are shown by the black dashed lines to measure the uncertainties. We then fit our two-component model to the observed and the bootstrap density distributions, and the inner 68% of the best-fitting models (determined by means of the least square method) are shown by the orange band. The lower half of the panels of Fig. 2 illustrate the corresponding $\lambda_{R_e,intr}$ distributions of the best-fitting two-component models, denoted with the relative percentage of the two distinct kinematic populations with intrinsically faster and slower rotation.

The estimated distributions of $\lambda_{R_e,intr}$ in the lower panels of Fig. 2 do not differ significantly from the observed λ_{R_e} distributions above, which indicates a weak projection effect overall. By showing the bimodality variation as a function of star-formation levels, the lower panels of Fig. 2 indicate that the two kinematic populations are most distinct with comparable importance when galaxies are massive and of intermediate star formation (GV and $\mathcal{M}_\star > 10^{10.8}\mathcal{M}_\odot$). The fraction of galaxy population with slower rotation generally increases with increasing stellar mass and decreasing SFR, ranging from 5% to 10% among SF galaxies of relatively low mass to 65% among most massive PS galaxies. The slow-rotating populations only make up a minority in a large mass range below $10^{11}\,\mathcal{M}_\odot$ (see also Fig. 13 of ref. 12 and Fig. 3 of ref. 15).

The non-negligible fractions of the intrinsically slow-rotating population among SF galaxies indicate that the tails of the observed λ_{R_e} distributions of SF galaxies are not merely due to projection effect (that is, not just face-on disks). This can also be seen in Extended Data Fig. 1, which shows the distributions on the λ_{R_e} versus ε diagram for galaxy subsamples as in Fig. 2. Among SF galaxies in the upper row (represented by black dots), for those that have low values of apparent λ_{R_e} (for example, $\lambda_{R_e} < 0.4$), some of them do have fairly round shapes
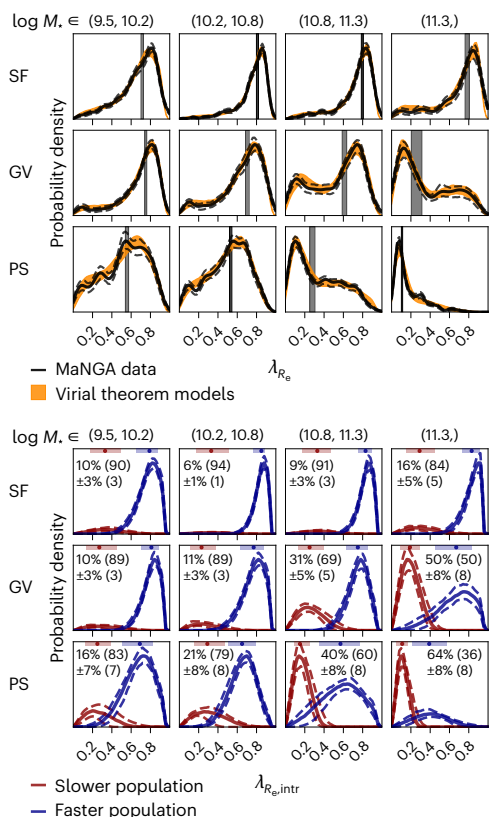
Fig. 2 | The observed distributions of stellar spin λ_{R_e} and the corresponding modelled distributions of the inclination corrected intrinsic stellar spin $\lambda_{R_e,intr}$. Upper half, the black solid line in each panel is the observed λ_{R_e} density distribution of MaNGA galaxies in a certain bin of stellar mass and star formation level, with its uncertainty shown by the black dashed lines which illustrate the inner 68% (in between 16% and 84% percentiles) of the density profiles of one hundred bootstrap samples. The range covered by the inner 68% of all median λ_{R_e} of individual bootstrap samples is illustrated by a grey vertical band. The orange band shows the inner 68% of the density profiles of the best-fitting models (models of two kinematic populations in virial equilibrium) for the MaNGA and bootstrap samples. As denoted, the stellar mass of each column increases rightward, and the star formation level of each row decreases downward from SF to GV and to PS. Lower half, the $\lambda_{R_e,intr}$ distribution and its uncertainty of the best-fitting models for the two kinematic populations in the model with intrinsically faster (blue lines) and slower (red lines) rotation. In each panel, the numbers are fractions with error of the slow-rotating (fast-rotating) populations, and the dotted bars at the top edge show the median positions (the dot) and the inner 68% of the two density distributions.

with little ε and are consistent with being face-on disks, that is, those that are connected with relatively edge-on disks at $\lambda_{R_e} \approx \varepsilon \approx 0.8$ by the black dotted lines predicted by the tensor virial theorem. But many more galaxies in the low-λ_{R_e} regime are too flattened to be face-on disks. More importantly, if not decisively, in the following, we will see that the slow-rotating populations manifest drastically different stellar-population properties from their fast-rotating counterparts. This argues strongly against the possibility that the SF slow-rotating populations are contaminated largely by face-on disks, in which case there should be no significant difference in the stellar populations of SF slow- and fast-rotating galaxies. Unlike the archetypical slow rotators among massive PS galaxies (predominantly occupying the lower left trapezium area in Extended Data Fig. 1), the SF slow-rotating populations may generally possess residual disc structure (for example, counterrotating disks as seen from the kinematic maps), similar to the low-mass, slow-rotating, early-type galaxies studied in ref. 28.

Notably, with decreasing SFR, the lower panels of Fig. 2 show that the $\lambda_{R_e,intr}$ distributions of the fast-rotating populations broaden and move towards lower values, as shown by the dotted bars at the upper edge of panels which mark the position and width of the distributions. This phenomenon is more obvious at higher stellar mass. Massive slow-rotating populations further lose their residual angular momenta as they quench the star formation, and the oldest PS systems among them have spiked $\lambda_{R_e,intr}$ distributions that are concentrated at values close to zero. These trends of higher-order terms can be also seen in the apparent λ_{R_e} distributions.

We find that the bimodality persists in diverse environments, quantified, for example, by the mass of dark matter halos from the catalogue[29] based on abundance matching, or by nearest neighbours defined number densities[30] that reflect more about the local environment. With the dedicated group catalogue[30] for MaNGA galaxies, Extended Data Fig. 2 shows the variation of bimodality between large (the left-hand side panels; the number of group members $\mathcal{N} \geq 6$) and small galaxy groups (the right-hand side panels; $\mathcal{N} < 6$), for galaxies in the same bins as in Fig. 2. The parameter $\mathcal{N}$ not only indicates the galaxy richness in a group but is also a good indicator of the mass of dark matter halos, with a Spearman rank correlation coefficient between the two of ~0.9. The specific definition of large and small groups is made by considering that the median galaxy groups in our sample host about six members. Extended Data Fig. 2 shows that the marked bimodal populations among massive GV galaxies appear to be even more distinct in larger galaxy groups. For SF low-mass galaxies, intriguingly, the fraction of the slow-rotating population in larger groups is nearly zero and is clearly lower than in smaller groups, which can also be seen from the observed λ_{R_e} distributions alone.

The drastically different kinematics of the two populations at the same mass and SFR implies at least two divergent evolution pathways. We first probe their recent star formation histories (SFHs) using measurements that indicate SFRs, respectively, over short and long timescales. The luminosity of Hα emission line can trace the ionizing photons emitted by the most massive and short-lived stars, and thus the SFR over recent ~10 Myr. The SFRs based on UV to mid-IR SED are averaged over 100 Myr, a timescale close to the lifespan of young stars that emit mainly in the UV wavelength. Galaxies with smooth SFHs such as a gradual decline of SFR will show consistent values of Hα luminosity and UV-based SFR, and those with fast-changing SFHs such as burst or fast cessation of star formation can produce incompatible Hα luminosity and UV-based SFRs, which occurs when most massive stars in the young stellar populations have died.

The circles in Fig. 3 show the MaNGA galaxies on the Hα luminosity $L_{H\alpha}$ versus SFR diagram, separately for SF (upper panels) and GV (lower panels) galaxies in four different mass bins. Each galaxy is colour coded by $\lambda_{R_e} - \langle\lambda_{R_e}\rangle$, where $\langle\lambda_{R_e}\rangle$ is the value averaged over galaxies of similar $\mathcal{M}_\star$ and SFR by means of the locally weighted regression method LOESS[31]. We have also implemented LOESS in each panel of Fig. 3 to uncover the mean trend. The Hα is integrated within $1.5R_e$ which is the observation coverage for the majority of MaNGA galaxies, regardless of the ionization type. The results are consistent if we include only high S/N emissions with unambiguous star-formation origin according to the BPT diagram[32,33] of O_{III}/H_β versus N_{II}/H_α diagnostics, and take extinction into account. The PS galaxies are not shown here because of their low Hα luminosity and large uncertainties in SFRs.

The grey lines, marking the contours enclosing 90%, 68% and 20% of all galaxies studied in Fig. 3, show a clear correlation between Hα-based and UV-based SFRs. This means that a sharp transition in the overall star formation of galaxies is not common at low redshift. There are still several SF galaxies with low Hα luminosity deviating from the main trend, seemingly more at the low- and high-mass ends, and the fraction of deviating galaxies clearly increases in the GV. Notably, galaxies on the main correlation denoted by the grey contours are mostly fast rotating with positive $\lambda_{R_e} - \langle\lambda_{R_e}\rangle$, whereas those deviating from
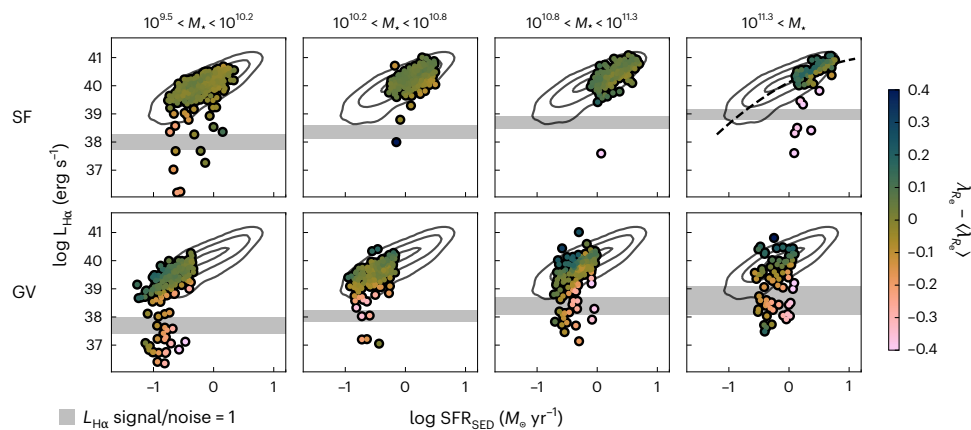
Fig. 3 | The correlation between stellar angular momentum and recent SFH. Each panel shows, on a logarithmic scale, the integrated luminosity of Hα emission line (SFR over short timescale) versus SFR derived from UV, optical and mid-IR SED (SFR over long timescale) for MaNGA galaxies in a certain bin of mass- and star-formation level (bins are the same as in Fig. 2 except that PS galaxies are not displayed due to their large errors on both axes). The grey horizontal band in each panel shows the noise level, represented by 1σ width of the distribution of integrated (over pixels within $1.5 R_e$) Hα line noise. Data points are colour coded by the spin difference from the average at the mass and SFR of the galaxy, with LOESS smoothing applied to emphasize the trend that galaxies of lower spin tend to have lower Hα luminosity. The scatter from this mean trend is presented in Extended Data Fig. 3. The grey lines, the same in every panel, are contours enclosing 90%, 68% and 20% of all galaxies in this figure, showing the general consistency between SFRs over short and long timescales.

this correlation rotate more slowly with negative $\lambda_{R_e} - \langle\lambda_{R_e}\rangle$ values. Extended Data Fig. 3 confirms the result, under no LOESS smoothing, by directly showing $\lambda_{R_e} - \langle\lambda_{R_e}\rangle$ versus $\log L_{H\alpha} - \langle\log L_{H\alpha}\rangle$ for each galaxy, where the latter quantifies the deviation of Hα luminosity from the mean trend (the quadratic fit to all galaxies shown by the black dashed curve in the upper rightmost panel of Fig. 3). The fraction of galaxies with smaller spin, or of the classic slow rotators (defined by equation 19 of ref. 11) as marked by the red circles, generally increases when the Hα emissions of galaxies are less luminous than the population average. This trend indicates that fast cessation of star formation is more common in the population with slower rotation, which is consistent with previous works[34,35].

We further explore the SFHs of the fast- and slow-rotating population using stellar metallicity. The stellar metallicity difference between SF and PS galaxies is an effective indicator for differentiating different quenching scenarios[36]. Rapid removal of gas through strong outflows or stripping can produce a passive galaxy with similar stellar metallicity as its SF progenitor. However, the star formation of galaxies without gas supply, that is, galaxies in so-called starvation[37], reduces gradually and elevates the average stellar metallicity by the enriched interstellar medium. This idea has been applied to large samples of galaxies in the local Universe[38].

Figure 4 shows the stellar metallicity versus stellar mass relationship, respectively, for galaxies with faster (left-hand panel) and slower (right-hand panel) rotation, and separately for different star-formation states as denoted in the upper-left-hand corner. Each point with an error bar represents the median value and its uncertainty is measured by the standard deviation of 1,000 bootstrap samples. The stellar metallicity measurements normalized to the solar value $Z/Z_\odot$ are taken from the PIPE3D value-added catalogue for MaNGA galaxies[39,40]. These light-weighted measurements based on full-spectrum fitting are all derived at one half-light radius R_e from line fitting to the metallicity radial profiles, so that they enable fair comparison between galaxies of different sizes while being representative of average metallicity over galactic scale[41]. Galaxies are divided into faster and slower population by their location relative to the λ_{R_e} versus ε relation predicted by the tensor virial theorem for a galaxy with $\lambda_{R,\text{intr}} = 0.4$ (corresponding to $\varepsilon_{\text{intr}} = 0.525$ and $\delta = 0.7\varepsilon_{\text{intr}} = 0.367$) projected at all inclinations. The demarcation $\lambda_{R,\text{intr}} = 0.4$ is close to the distribution intersection in all but the lower right panels of the lower half of Fig. 2. We note that this demarcation is empirically based on the bimodal distributions and is

notably higher than that for the classic slow rotators which are maximally spheroid-dominated systems. Therefore, the slower population includes both the classic slow rotators and spheroid-dominated galaxies but with residual disc components. The following result remains qualitatively the same if we study the radial profiles of metallicity, use the latest FIREFLY light-weighted metallicity measurements[42,43] or adopt the classic fast- and slow-rotator classification.

Among the galaxy population with faster rotation, the stellar metallicity shows a significant increase with decreasing star formation at all masses. By contrast, within errors, the stellar metallicity of the galaxy population with slower rotation does not depend on star formation, except that the low-mass SF galaxies are relatively metal poor at the given mass. The PS slow-rotating populations are markedly less enriched than their fast-rotating counterparts. Although minor mergers are able to develop metal-poor envelopes at the very outskirt of massive elliptical galaxies, they can hardly affect the main stellar body in the inner part[44], which makes the merger history an implausible reason for the observed metallicity difference. Recent works[45,46] show that smaller galaxies with deeper gravitational potential wells may be enriched more efficiently. We find that slow-rotating galaxies are generally more compact (smaller R_e) than fast-rotating counterparts. If potential does play a dominant role in the metal-enrichment history (this is under debate; see, for example, ref. 47), then the deeper potential of the PS slow-rotating population yet with lower metallicity particularly elevates the importance of the quenching history in explaining their chemical property. Together, these results fit well in the scenario of quenching histories[36] and suggest that the fast-rotating galaxies are primarily quenched through starvation, whereas for the slow-rotating population this is through rapid gas removal.

The links between stellar angular momentum and SFHs might be natural consequences if disks grow quietly in quasi-equilibrium out of smooth and gradual gas inflows[48,49] and spheroids build up in disruptive and chaotic processes, such as mergers and violent disc instability[50–54]. Star formation in fast-rotating galaxies can be quenched by preventive feedback[4,55] or quenched when gas is accreted with excessive angular momentum that hinders adequate radial inflows[56]. In both cases, the quenching proceeds slowly under starvation, with concurrent stellar metallicity enrichment. However, for the slow-rotating population, when massive dark matter halos are present[57,58], the violent processes they experience are able to halt the star formation in a short time by

gas depletion due to both star bursts and massive outflows[59,60], leaving stars less enriched in the end.

In this picture, it is expected that the fraction of slow-rotating massive galaxies increases sharply from SF to GV, as shown in Fig. 2, given the presumably high quenching probability after violent events. The highest peak of low $\lambda_{R_e,\mathrm{intr}}$ among most massive PS galaxies is observed and anticipated as these galaxies formed in the high peaks of the primordial density field with subsequent numerous mergers because of their gravitational dominance in the large-scale structure[61]. Over the relatively quiet formation history of disc populations, they could not always avoid disturbance and heating by external galaxy interactions and internal non-axisymmetric structures, which explains the broadening and moving of the peak of high $\lambda_{R_e,\mathrm{intr}}$ with decreasing SFR. However, compared with massive galaxies, the weaker kinematic bimodality of low-mass galaxies implies more diverse formation histories[28], possibly due to their vulnerability to all kinds of effects. For example, accretion of gas with misaligned angular momentum and its fuelled star formation can slow down the average rotational velocity of stellar populations[49]. Also, gravitational interactions with giant galaxies can heat the stars of low-mass satellites. These interactions, although not as devastating as mergers, may modestly reduce the rotational support of low-mass galaxies and make them kinematically intermediate systems.

To conclude, in this work we highlight the galaxy bimodality in kinematic morphology across different star-formation levels in the local Universe, which is most significant for massive galaxies of intermediate star formation. This ubiquitous kinematic bimodality, present also among galaxies of different masses and in diverse environments, moves a step further from the acknowledged fast- and slow-rotator dichotomy[10–13], and proves to be a general and fundamental property of galaxy populations.

Recent works[14,15] suggest that a simple bimodal description of galaxy stellar kinematics using two Gaussian components is not applicable for all galaxies and galaxy populations at certain stellar masses. Our results suggest that this can be understood given that the fast- and slow-rotating modes of the $\lambda_{R_e,\mathrm{intr}}$ Gaussian components systematically vary with SFR. Most notably, the old and passive fast-rotating populations are dynamically hotter and have less angular momentum than their young and SF counterparts, which blurs the bimodality when galaxies of comparable mass but different SFR are viewed together.

It has long been suggested that the transitional galaxies in the GV are typically disc plus spheroid composites with intermediate spheroid/total mass ratio, like the Sombrero Galaxy. The suggestion comes from the well-established empirical correlation between morphology and star-formation level of galaxies[62–65], where transitional galaxies have intermediate morphology on average. Nevertheless, our results show that the average morphology, in particular, for the massive transitional population, is not a valid representation of the underlying galaxy populations. The kinematic bimodality indicates that the galaxies are closer to being either disks or spheroids than being composite systems in between. The associated distinctions in metal enrichment and recent SFHs provide further evidence for the existence of two kinematic populations at certain mass and SFR, respectively, with quiet and violent formation and quenching histories.

Quenching in the local Universe is thus rarely happening in galaxies comprising a slow-rotating bulge and a fast-rotating disc of comparable mass. As opposed to previous belief, apart from the extremely massive galaxies, the quenching of star formation at low redshifts are proceeding mostly in disc galaxies that are kinematically akin to common blue galaxies of vigorous star formation. Towards the high-mass end, the sharply growing prevalence of quenching by means of the slow-rotating channel is reminiscent of the significant increase of ex situ mass (that is, from mergers) fraction with galaxy mass[66]. After a galaxy is quenched, it loses the ability to maintain or rebuild a disc by means of star formation, and hence embarks upon a one-way trip

to lower rotation unless it absorbs a large amount of orbital angular momentum from mergers of specific configurations.

Massive galaxies are luminous representatives of the overall cosmic structure. Their unambiguous bimodal kinematic morphology, and the contrasting quenching histories associated with the two kinematic modes, imply the existence of divergent evolution pathways in the formation of the cosmos. State-of-the-art simulations suggest a wide range of factors that together decide the stellar kinematics of galaxies, including halo spin, properties of mergers (for example, orbital configurations, wetness and mass ratios) and tidal interactions with the environment[67–69]. But none of these properties appears to be bimodal, nor have simulations directly shown such bimodal kinematics among massive galaxies[14,70]. Future large surveys of integral field spectroscopy at higher redshifts may provide key clues by showing the temporal evolution of the kinematic bimodality, which carries indispensable information about how galaxies were formed.

Methods
The galaxy sample
We take integral field spectroscopy data from the MaNGA survey, the part in the publicly available SDSS Data Release 15 (ref. 16). This data release includes 4,597 unique galaxies in the redshift range $0.01 < z < 0.15$ observed by means of hexagonal integral field units with angular resolution full-width at half-maximum of 2.5 arcsec and effective diameters ranging from 12 to 32 arcsec[71]. The spectra cover from 360 to 1,030 nm with median instrument broadening $\sigma_{\mathrm{inst}} \approx 72\ \mathrm{km\ s^{-1}}$ (ref. 72) and typical spectral resolution $R \approx 2,000$.

Our data are included in the three major subsamples[73] of the MaNGA survey. The primary and secondary subsample are selected to ensure spatial coverage, respectively, out to 1.5 and 2.5 half-light radii R_e, with a flat mass distribution. The colour-enhanced subsample is designed to increase the number of galaxies in the low-density regions of the colour–magnitude diagram by extending the redshift limits of the primary subsample in appropriate colour bins, so that the primary plus the colour-enhanced subsamples smoothly cover the colour–magnitude diagram. No cuts are applied to galaxy colour, morphology or environment so that MaNGA galaxies are fully representative of galaxy population in the local Universe.

We apply the same data quality control as in ref. 12, to remove data that are flagged as being bad or show signs of being problematic, and to exclude galaxies that are too small compared with the MaNGA synthesized beam. Visually checking the SDSS optical images, galaxies in close pairs are excluded when their stellar light is highly blended with the half-light ellipses hard to define. Overlapping merging galaxies in chaotic morphology, that is, ongoing mergers with low mass difference, are not included as they are far from being dynamically relaxed and the stellar kinematics is overwhelmed by the orbital motion between the galaxies rather than the internal stellar motion. Our sample captures the post-merger phases when galaxies have roughly resumed dynamical equilibrium. The above control discards 12% of all galaxies and is meant for robust quantifications of internal stellar kinematics. After cross matching with the GALEX-SDSS-WISE Legacy Catalogue[18,19] of total stellar mass and SFR for SDSS galaxies, we finally reach a sample of 3,279 galaxies among which 2,981 galaxies have stellar mass above $10^{9.5}\ \mathcal{M}_\odot$.

In the consensus cosmology, mergers play an important role in galaxy evolution[74]. Removing the currently merging galaxies, which only make up a small fraction (3%), certainly does not mean that the populations studied have not been affected by mergers in the past. Supplementary Fig. 1 shows the asymmetry of galaxy shapes under 180-degree rotation[75] for fast- and slow-rotating galaxies in different star-formation states. Across a large range of stellar masses, the shape asymmetry remains consistently at low levels (comparable to the median values of galaxies with regular morphologies presented by the panels (b) of Figure 11 in ref. 75), suggesting that galaxies in our
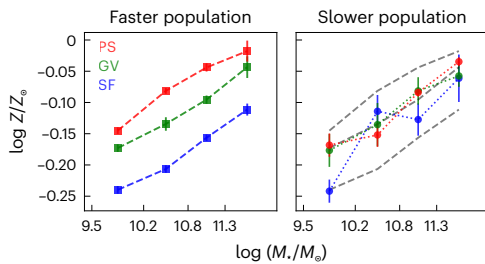
Fig. 4 | The stellar metallicity versus mass relationship for the two kinematic populations. Left, the relationship for MaNGA galaxies with $\lambda_{R_e,\text{intr}} > 0.4$, divided into star-formation levels of SF, GV and PS with different colours as labelled in the upper-left-hand corner. The mass bins are the same as in previous figures. Right, the relationships for those with $\lambda_{R_e,\text{intr}} < 0.4$, with the same star formation and mass binning as for those in the left-hand panel. Additionally, the median relationships in the left-hand panel, for the population that rotate faster, are also overlaid here for direct comparison. In both panels, each data point shows the median value with an error represented by the standard deviation of 1,000 bootstrap resamplings. Sizes of the samples used for statistics, from low to high mass, are shown in the following brackets: the faster population—SF (441/310/233/77), GV (183/160/127/35), PS (138/258/168/40); the slower population—SF (27/7/8/9), GV (18/21/38/33), PS (39/70/162/176). The results stay markedly consistent with the latest MaNGA data, which more than doubles the size of each sample studied here.

sample that are severely out of dynamical equilibrium are rare, which is a consequence expected for our quality control. But inspection of optical images[76] reveals the presence of tidal debris (for example, shells, streams and tails) among a significant fraction of these galaxies, and this indicates the occurrence of merger events in the near past[77]. Of the SF, fast-rotating galaxies, 12% have visually identified tidal features, and this number almost doubles (21%) for SF, slow-rotating galaxies, for which we indeed expect more mergers. We note that the above fractions are only lower limits given the finite depth of the imaging data.

The spin parameter λ_{R_e}

We use λ_{R_e} to quantify the level of rotational support of galaxies. The stellar kinematics can better reflect the intrinsic morphology of galaxies than projected light distributions[11], so that the quantification λ_{R_e} is also referred to as a parameter of kinematic morphology.

The measurements of λ_{R_e} for MaNGA galaxies are taken from ref. 17 with the methods detailed in ref. 12. The maps of stellar kinematics in the MAPS files are produced by the Data Analysis Pipeline of MaNGA[78]. The Data Analysis Pipeline first Voronoi bins[79] the data cubes to achieve a minimum signal-to-noise ratio of ~10 per spectral bin of width 70 km s^{-1}. Then, the penalized pixel-fitting method[80] is applied to extract the line-of-sight velocity distribution by fitting a set of 49 families of stellar spectra from the MILES stellar library[81,82] to the observed absorption-line spectra, from where one can characterize the stellar kinematics by the mean stellar velocity V and velocity dispersion σ. The value of λ_{R_e} is calculated using equations 5 and 6 of ref. 25:

$$\lambda_R \equiv \frac{\langle R\,|V|\rangle}{\langle R\sqrt{V^2+\sigma^2}\rangle} = \frac{\sum_{n=1}^{N} F_n R_n |V_n|}{\sum_{n=1}^{N} F_n R_n \sqrt{V_n^2+\sigma_n^2}} \tag{1}$$

where F_n, V_n, and σ_n are the flux, mean velocity and velocity dispersion of the nth pixel. The summation is performed over the N pixels within radius R, and, specifically for this work, within the elliptical half-light radius R_e for λ_{R_e}.

Seeing corrections for the observed λ_{R_e} have been applied using analytic functions[12]. Briefly, the effect of atmospheric smearing is quantified by measuring λ_{R_e} of realistic models of galaxy kinematics[83] convolved with a Gaussian point spread function (PSF) of varying

widths. An independent test[84] shows that the correction is effective and leaves little systematics. About 3% of our galaxies have $\sigma_{\text{PSF}}/R_e^{\text{maj}} > 0.5$, which get large correction for smearing. The correction is only effective for and applied to galaxies with regular, hourglass-like rotation in their velocity field. Non-regular rotator galaxies are mostly slow rotating with median $\lambda_{R_e} = 0.07$ and their underestimation of λ_{R_e} due to smearing is generally at the level of 0.1 (ref. 85).

Ellipticity ε

With the predictions from the tensor virial theorem, we use the observed ellipticity ε of galaxy shape along with the measured λ_{R_e} to broadly classify galaxies into intrinsically flat and round objects (in Fig. 4). The ellipticity, catalogued in ref. 17, is measured by modelling the SDSS r-band photometry by means of the multi-Gaussian expansion method[86,87].

The ellipticity is calculated inside the model half-light isophote from the second moments of light distribution:

$$(1-\varepsilon)^2 = q'^2 = \frac{\langle y^2\rangle}{\langle x^2\rangle} = \frac{\sum_{k=1}^{P} F_k y_k^2}{\sum_{k=1}^{P} F_k x_k^2} \tag{2}$$

where F_k and (x_k, y_k) are the flux and coordinate of the kth pixel, respectively.

Kinematic models

We build kinematic models of axisymmetric galaxies by means of the tensor virial theorem[24], which predicts the ordered to random motion ratio $(V/\sigma)_{\text{intr}}$ with given intrinsic shape $\varepsilon_{\text{intr}}$ and velocity anisotropy δ. The formalism is summarized by equations 14 and 15 of ref. 11. The predicted $(V/\sigma)_{\text{intr}}$ is then translated into $\lambda_{R,\text{intr}}$ using the tight relationship derived from two-integral Jeans models[10].

We assume, for our theoretical galaxy populations, that their $\varepsilon_{\text{intr}}$ distribution, in the range (0, 1), is composed of two Gaussians truncated at zero and one. With the sampled $\varepsilon_{\text{intr}}$ from the two-Gaussian distribution, we assign each model galaxy the velocity anisotropy δ randomly sampled from a uniform distribution in the empirically motivated range $[0, 0.7\varepsilon_{\text{intr}}]$ (refs. 88,89). The $\lambda_{R,\text{intr}}$ can then be calculated for each galaxy in the model galaxy population, which are later projected onto the sky plane at random orientation using equation 16 of ref. 11. We finally arrive at the projected λ_R distribution of the model galaxy population to be compared with observations.

When fitted to the data, the five free parameters of our theoretical galaxy population are the positions (two parameters), standard deviations (two parameters) and fractions (one parameter) of the two Gaussian components in the assumed $\varepsilon_{\text{intr}}$ probability density distribution.

SFR and stellar mass

These two measurements are provided by the version X2 of the GALEX-SDSS-WISE Legacy Catalogue[18,19] (GSWLC-X2) for SDSS galaxies in redshift range $0.01 < z < 0.3$ within the footprint of the GALEX All-sky Imaging Survey[90]. Using the state-of-the-art modelling technique[91,92] (CIGALE), stellar mass and SFR are derived by fitting the SED of two GALEX UV flux, five SDSS optical plus near-IR flux and one mid-IR flux (22 microns or 12 microns when the former is not available) from the Wide-field Infrared Survey Explorer (WISE)[93]. A Chabrier[94] initial mass function and a flat WMAP7 cosmology ($H_0 = 70$ km s^{-1} Mpc^{-1}, $\Omega_m = 0.27$) are assumed. There are deeper GALEX UV observations nested in the All-sky Imaging footprint, and GSWLC-X2 makes use of the deepest available UV image for each galaxy. Note that GSWLC masses are systematically smaller than the dynamically calibrated masses[95] by ~0.4 dex. This means that the characteristic mass $\mathcal{M}_{\text{crit}} \approx 10^{11.3}$ (ref. 11), where slow rotators start dominating, appears at $\mathcal{M}_{\text{crit}} \approx 10^{10.9}$ in our sample.

Stellar metallicity

From the MaNGA-PIPE3D value-added catalogue, we retrieve the light-weighted stellar metallicity measurements at one R_e. The IA-UNAM MaNGA team created the catalogue by analysing the MaNGA data cubes through the PIPE3D pipeline[39,96], which fits the stellar continuum with stellar-population models and measures the nebular emission lines of galaxies. A Salpeter[97] initial mass function and a standard ΛCDM cosmology ($H_0 = 73$ km s^{-1} Mpc^{-1}, $\Omega_m = 0.3$) are assumed. PIPE3D has been extensively tested against other spectrum fitting tools, and widely used in many other integral field spectroscopy surveys.

The stellar metallicity values at one R_e are derived according to the linear regression of metallicity radial profiles and have been shown to match well the average metallicity across the optical extension of galaxies and with less error[41]. We find consistent results by using mass-weighted metallicity or analysing metallicity profiles.

Data availability

The MaNGA DR15 MAPS files of spatially resolved emission line properties and stellar kinematics are archived at https://dr15.sdss.org/sas/dr15/manga/spectro/analysis/v2_4_3/2.2.1/VOR10-GAU-MILESHC/. The measured λ_{R_e} and ε for MaNGA DR15 galaxies are catalogued in ref. 17, with the update to cover full MaNGA (DR17) recently published[60]. Stellar mass and SFR of the MaNGA galaxies are taken from the GSWLC-X2 catalogue[18,19] available on https://salims.pages.iu.edu/gswlc/. The stellar metallicity measurements[39,40] that we use are publicly available on https://www.sdss.org/dr15/manga/manga-data/manga-pipe3d-value-added-catalog/. The shape asymmetry quantifications[75] are taken from https://www.sdss4.org/dr17/data_access/value-added-catalogs/?vac_id=pawlikmorph-catalog-of-galaxy-morphologies. The visual identifications of tidal debris[76] are retrieved from the catalogue at https://www.sdss4.org/dr17/data_access/value-added-catalogs/?vac_id=manga-visual-morphologies-from-sdss-and-desi-images.

Code availability

We use the Python package LOESS v.2.0.11 available from https://pypi.org/project/loess/ to apply the locally weighted regression method LOESS[31]. The MGEFIT Python software package used for multi-Gaussian expansion[86,87] of galaxy surface brightness is available at https://pypi.org/project/mgefit/. The isophotal contour containing half the total luminosity of the multi-Gaussian expansion model is determined via the routine MGE_HALF_LIGHT_ISOPHOTE, which is included in the JAMPY Python software package[83] available at https://pypi.org/project/jampy/.

References

1. Fall, S. M. & Efstathiou, G. Formation and rotation of disc galaxies with haloes. *Mon. Not. R. Astron. Soc.* **193**, 189–206 (1980).
2. Mo, H. J., Mao, S. & White, S. D. M. The formation of galactic discs. *Mon. Not. R. Astron. Soc.* **295**, 319–336 (1998).
3. Dekel, A. & Burkert, A. Wet disc contraction to galactic blue nuggets and quenching to red nuggets. *Mon. Not. R. Astron. Soc.* **438**, 1870–1879 (2014).
4. Somerville, R. S. & Davé, R. Physical models of galaxy formation in a cosmological framework. *Annu. Rev. Astron. Astrophys.* **53**, 51–113 (2015).
5. de Zeeuw, P. T. et al. The SAURON project—II. Sample and early results. *Mon. Not. R. Astron. Soc.* **329**, 513–530 (2002).
6. Cappellari, M. et al. The ATLAS3D project—I. A volume-limited sample of 260 nearby early-type galaxies: science goals and selection criteria. *Mon. Not. R. Astron. Soc.* **413**, 813–836 (2011).
7. Sánchez, S. F. et al. CALIFA, the Calar Alto Legacy Integral Field Area survey. I. Survey presentation. *Astron. Astrophys.* **538**, A8 (2012).
8. Bryant, J. J. et al. The SAMI Galaxy Survey: instrument specification and target selection. *Mon. Not. R. Astron. Soc.* **447**, 2857–2879 (2015).
9. Bundy, K. et al. Overview of the SDSS-IV MaNGA survey: mapping nearby galaxies at Apache Point Observatory. *Astrophys. J.* **798**, 7 (2015).
10. Emsellem, E. et al. The ATLAS3D project—III. A census of the stellar angular momentum within the effective radius of early-type galaxies: unveiling the distribution of fast and slow rotators. *Mon. Not. R. Astron. Soc.* **414**, 888–912 (2011).
11. Cappellari, M. Structure and kinematics of early-type galaxies from integral field spectroscopy. *Annu. Rev. Astron. Astrophys.* **54**, 597–665 (2016).
12. Graham, M. T. et al. SDSS-IV MaNGA: stellar angular momentum of about 2300 galaxies: unveiling the bimodality of massive galaxy properties. *Mon. Not. R. Astron. Soc.* **477**, 4711–4737 (2018).
13. Wang, B., Cappellari, M., Peng, Y. & Graham, M. SDSS-IV MaNGA: the kinematic-morphology of galaxies on the mass versus star-formation relation in different environments. *Mon. Not. R. Astron. Soc.* **495**, 1958–1977 (2020).
14. van de Sande, J. et al. The SAMI Galaxy Survey: a statistical approach to an optimal classification of stellar kinematics in galaxy surveys. *Mon. Not. R. Astron. Soc.* **505**, 3078–3106 (2021).
15. Fraser-McKelvie, A. & Cortese, L. Beyond galaxy bimodality: the complex interplay between kinematic morphology and star formation in the local Universe. *Astrophys. J.* **937**, 117 (2022).
16. Aguado, D. S. et al. The fifteenth data release of the Sloan Digital Sky Surveys: first release of MaNGA-derived quantities, data visualization tools, and stellar library. *Astrophys. J. Suppl. Ser.* **240**, 23 (2019).
17. Bevacqua, D., Cappellari, M. & Pellegrini, S. SDSS-IV MaNGA: integral-field kinematics and stellar population of a sample of galaxies with counter-rotating stellar discs selected from about 4000 galaxies. *Mon. Not. R. Astron. Soc.* **511**, 139–157 (2022).
18. Salim, S. et al. GALEX-SDSS-WISE Legacy Catalog (GSWLC): star formation rates, stellar masses, and dust attenuations of 700,000 low-redshift galaxies. *Astrophys. J. Suppl. Ser.* **227**, 2 (2016).
19. Salim, S., Boquien, M. & Lee, J. C. Dust attenuation curves in the local Universe: demographics and new laws for star-forming galaxies and high-redshift analogs. *Astrophys. J.* **859**, 11 (2018).
20. Strauss, M. A. et al. Spectroscopic target selection in the Sloan Digital Sky Survey: the main galaxy sample. *Astron. J.* **124**, 1810–1824 (2002).
21. Renzini, A. & Peng, Y. An objective definition for the main sequence of star-forming galaxies. *Astrophys. J. Lett.* **801**, L29 (2015).
22. Lilly, S. J., Carollo, C. M., Pipino, A., Renzini, A. & Peng, Y. Gas regulation of galaxies: the evolution of the cosmic specific star formation rate, the metallicity-mass-star-formation rate relation, and the stellar content of halos. *Astrophys. J.* **772**, 119 (2013).
23. Peng, Y. & Maiolino, R. From haloes to galaxies—I. The dynamics of the gas regulator model and the implied cosmic sSFR history. *Mon. Not. R. Astron. Soc.* **443**, 3643–3664 (2014).
24. Binney, J. Rotation and anisotropy of galaxies revisited. *Mon. Not. R. Astron. Soc.* **363**, 937–942 (2005).
25. Emsellem, E. et al. The SAURON project – IX. A kinematic classification for early-type galaxies. *Mon. Not. R. Astron. Soc.* **379**, 401–417 (2007).
26. van de Sande, J. et al. A relation between the characteristic stellar ages of galaxies and their intrinsic shapes. *Nature Astronomy* **2**, 483–488 (2018).
27. Weijmans, A.-M. et al. The ATLAS3D project—XXIV. The intrinsic shape distribution of early-type galaxies. *Mon. Not. R. Astron. Soc.* **444**, 3340–3356 (2014).

28. Krajnović, D. et al. Formation channels of slowly rotating early-type galaxies. *Astron. Astrophys.* **635**, A129 (2020).

29. Yang, X. et al. Galaxy groups in the SDSS DR4. I. The catalog and basic properties. *Astrophys. J.* **671**, 153–170 (2007).

30. Graham, M. T., Cappellari, M., Bershady, M. A. & Drory, N. SDSS-IV MaNGA: complete census of massive slow-rotator early-type galaxy candidates and their environment in a volume-limited sample. Preprint at https://arXiv.org/abs/1910.05136 (2019).

31. Cappellari, M. et al. The ATLAS3D project—XX. Mass-size and mass-σ distributions of early-type galaxies: bulge fraction drives kinematics, mass-to-light ratio, molecular gas fraction and stellar initial mass function. *Mon. Not. R. Astron. Soc.* **432**, 1862–1893 (2013).

32. Baldwin, J. A., Phillips, M. M. & Terlevich, R. Classification parameters for the emission-line spectra of extragalactic objects. *Publ. Astron. Soc. Pac.* **93**, 5–19 (1981).

33. Kauffmann, G. et al. The host galaxies of active galactic nuclei. *Mon. Not. R. Astron. Soc.* **346**, 1055–1077 (2003).

34. Schawinski, K. et al. The green valley is a red herring: Galaxy Zoo reveals two evolutionary pathways towards quenching of star formation in early- and late-type galaxies. *Mon. Not. R. Astron. Soc.* **440**, 889–907 (2014).

35. Smethurst, R. J. et al. SDSS-IV MaNGA: the different quenching histories of fast and slow rotators. *Mon. Not. R. Astron. Soc.* **473**, 2679–2687 (2018).

36. Peng, Y., Maiolino, R. & Cochrane, R. Strangulation as the primary mechanism for shutting down star formation in galaxies. *Nature* **521**, 192–195 (2015).

37. Larson, R. B., Tinsley, B. M. & Caldwell, C. N. The evolution of disk galaxies and the origin of S0 galaxies. *Astrophys. J.* **237**, 692–707 (1980).

38. Trussler, J. et al. Both starvation and outflows drive galaxy quenching. *Mon. Not. R. Astron. Soc.* **491**, 5406–5434 (2020).

39. Sánchez, S. F. et al. Pipe3D, a pipeline to analyze integral field spectroscopy data: II. Analysis sequence and CALIFA dataproducts. *Rev. Mexicana Astron. Astrofis.* **52**, 171–220 (2016).

40. Sánchez, S. F. et al. SDSS IV MaNGA—properties of AGN host galaxies. *Rev. Mexicana Astron. Astrofis.* **54**, 217–260 (2018).

41. Sánchez, S. F. et al. Mass-metallicity relation explored with CALIFA. I. Is there a dependence on the star-formation rate? *Astron. Astrophys.* **554**, A58 (2013).

42. Goddard, D. et al. SDSS-IV MaNGA: spatially resolved star formation histories in galaxies as a function of galaxy mass and type. *Mon. Not. R. Astron. Soc.* **466**, 4731–4758 (2017).

43. Neumann, J. et al. The MaNGA FIREFLY value added catalogue: resolved stellar populations of 10,010 nearby galaxies. *Mon. Not. R. Astron. Soc.* **513**, 5988–6012 (2022).

44. Du, M. et al. The evolutionary pathways of disk-, bulge-, and halo-dominated galaxies. *Astrophys. J.* **919**, 135 (2021).

45. Barone, T. M., D'Eugenio, F., Colless, M. & Scott, N. Gravitational potential and surface density drive stellar populations. II. Star-forming galaxies. *Astrophys. J.* **898**, 62 (2020).

46. Vaughan, S. P. et al. The SAMI galaxy survey: galaxy size can explain the offset between star-forming and passive galaxies in the mass-metallicity relationship. *Mon. Not. R. Astron. Soc.* **516**, 2971–2987 (2022).

47. Baker, W. M. & Maiolino, R. Stellar mass, not dynamical mass nor gravitational potential, drives the mass-metallicity relationship. *Mon. Not. R. Astron. Soc.* **521**, 4173–4179 (2023).

48. Renzini, A. On the angular momentum history of galactic discs. *Mon. Not. R. Astron. Soc.* **495**, L42–L45 (2020).

49. Park, M. et al. On the formation of massive quiescent galaxies with diverse morphologies in the TNG50 simulation. *Mon. Not. R. Astron. Soc.* **515**, 213–228 (2022).

50. Naab, T. et al. The ATLAS3D project—XXV. Two-dimensional kinematic analysis of simulated galaxies and the cosmological origin of fast and slow rotators. *Mon. Not. R. Astron. Soc.* **444**, 3357–3387 (2014).

51. Zolotov, A. et al. Compaction and quenching of high-z galaxies in cosmological simulations: blue and red nuggets. *Mon. Not. R. Astron. Soc.* **450**, 2327–2353 (2015).

52. Lagos, Cd. P. et al. Angular momentum evolution of galaxies in EAGLE. *Mon. Not. R. Astron. Soc.* **464**, 3850–3870 (2017).

53. Schulze, F. et al. Kinematics of simulated galaxies—I. Connecting dynamical and morphological properties of early-type galaxies at different redshifts. *Mon. Not. R. Astron. Soc.* **480**, 4636–4658 (2018).

54. Lagos, Cd. P. et al. The diverse nature and formation paths of slow rotator galaxies in the EAGLE simulations. *Mon. Not. R. Astron. Soc.* **509**, 4372–4391 (2022).

55. Croton, D. J. et al. The many lives of active galactic nuclei: cooling flows, black holes and the luminosities and colours of galaxies. *Mon. Not. R. Astron. Soc.* **365**, 11–28 (2006).

56. Peng, Y. & Renzini, A. Disc growth and quenching. *Mon. Not. R. Astron. Soc.* **491**, L51–L55 (2020).

57. Dekel, A. & Birnboim, Y. Galaxy bimodality due to cold flows and shock heating. *Mon. Not. R. Astron. Soc.* **368**, 2–20 (2006).

58. Tacchella, S. et al. The confinement of star-forming galaxies into a main sequence through episodes of gas compaction, depletion and replenishment. *Mon. Not. R. Astron. Soc.* **457**, 2790–2813 (2016).

59. Granato, G. L., De Zotti, G., Silva, L., Bressan, A. & Danese, L. A physical model for the coevolution of QSOs and their spheroidal hosts. *Astrophys. J.* **600**, 580–594 (2004).

60. Wang, B. & Peng, Y. The kinematic bimodality: efficient feedback and cold gas deficiency in slow-rotating galaxies. *Astrophys. J. Lett.* **950**, L22 (2023).

61. Cen, R. Gaussian random field: physical origin of Sersic profiles. *Astrophys. J. Lett.* **790**, L24 (2014).

62. Kauffmann, G. et al. The dependence of star formation history and internal structure on stellar mass for 10^5 low-redshift galaxies. *Mon. Not. R. Astron. Soc.* **341**, 54–69 (2003).

63. Baldry, I. K. et al. Quantifying the bimodal color-magnitude distribution of galaxies. *Astrophys. J.* **600**, 681–694 (2004).

64. Cameron, E., Driver, S. P., Graham, A. W. & Liske, J. The Millennium Galaxy Catalogue: exploring the color-concentration bimodality via bulge-disk decomposition. *Astrophys. J.* **699**, 105–117 (2009).

65. Bluck, A. F. L. et al. What shapes a galaxy?—unraveling the role of mass, environment, and star formation in forming galactic structure. *Mon. Not. R. Astron. Soc.* **485**, 666–696 (2019).

66. Tacchella, S. et al. Morphology and star formation in IllustrisTNG: the build-up of spheroids and discs. *Mon. Not. R. Astron. Soc.* **487**, 5416–5440 (2019).

67. Lagos, Cd. P. et al. The connection between mass, environment, and slow rotation in simulated galaxies. *Mon. Not. R. Astron. Soc.* **476**, 4327–4345 (2018).

68. Joshi, G. D. et al. The fate of disc galaxies in IllustrisTNG clusters. *Mon. Not. R. Astron. Soc.* **496**, 2673–2703 (2020).

69. Zeng, G., Wang, L. & Gao, L. Formation of massive disc galaxies in the IllustrisTNG simulation. *Mon. Not. R. Astron. Soc.* **507**, 3301–3311 (2021).

70. Peebles, P. J. E. Formation of the large nearby galaxies. *Mon. Not. R. Astron. Soc.* **498**, 4386–4395 (2020).

71. Drory, N. et al. The MaNGA integral field unit fiber feed system for the Sloan 2.5 m telescope. *Astron. J.* **149**, 77 (2015).

72. Law, D. R. et al. The Data Reduction Pipeline for the SDSS-IV MaNGA IFU galaxy survey. *Astron. J.* **152**, 83 (2016).

73. Wake, D. A. et al. The SDSS-IV MaNGA sample: design, optimization, and usage considerations. *Astron. J.* **154**, 86 (2017).

74. White, S. D. M. & Rees, M. J. Core condensation in heavy halos: a two-stage theory for galaxy formation and clustering. *Mon. Not. R. Astron. Soc.* **183**, 341–358 (1978).

75. Pawlik, M. M. et al. Shape asymmetry: a morphological indicator for automatic detection of galaxies in the post-coalescence merger stages. *Mon. Not. R. Astron. Soc.* **456**, 3032–3052 (2016).

76. Vázquez-Mata, J. A. et al. SDSS IV MaNGA: visual morphological and statistical characterization of the DR15 sample. *Mon. Not. R. Astron. Soc.* **512**, 2222–2244 (2022).

77. Johnston, K. V. et al. Tracing galaxy formation with stellar halos. II. Relating substructure in phase and abundance space to accretion histories. *Astrophys. J.* **689**, 936–957 (2008).

78. Westfall, K. B. et al. The data analysis pipeline for the SDSS-IV MaNGA IFU galaxy survey: overview. *Astron. J.* **158**, 231 (2019).

79. Cappellari, M. & Copin, Y. Adaptive spatial binning of integral-field spectroscopic data using Voronoi tessellations. *Mon. Not. R. Astron. Soc.* **342**, 345–354 (2003).

80. Cappellari, M. Improving the full spectrum fitting method: accurate convolution with Gauss–Hermite functions. *Mon. Not. R. Astron. Soc.* **466**, 798–811 (2017).

81. Sánchez-Blázquez, P. et al. Medium-resolution Isaac Newton Telescope library of empirical spectra. *Mon. Not. R. Astron. Soc.* **371**, 703–718 (2006).

82. Falcón-Barroso, J. et al. An updated MILES stellar library and stellar population models. *Astron. Astrophys.* **532**, A95 (2011).

83. Cappellari, M. Measuring the inclination and mass-to-light ratio of axisymmetric galaxies via anisotropic Jeans models of stellar kinematics. *Mon. Not. R. Astron. Soc.* **390**, 71–86 (2008).

84. Harborne, K. E., Power, C., Robotham, A. S. G., Cortese, L. & Taranu, D. S. A numerical twist on the spin parameter, λ_R. *Mon. Not. R. Astron. Soc.* **483**, 249–262 (2019).

85. Harborne, K. E. et al. Recovering λ_R and V/σ from seeing-dominated IFS data. *Mon. Not. R. Astron. Soc.* **497**, 2018–2038 (2020).

86. Emsellem, E., Monnet, G. & Bacon, R. The multi-Gaussian expansion method: a tool for building realistic photometric and kinematical models of stellar systems I. The formalism. *Astron. Astrophys.* **285**, 723–738 (1994).

87. Cappellari, M. Efficient multi-Gaussian expansion of galaxies. *Mon. Not. R. Astron. Soc.* **333**, 400–410 (2002).

88. Cappellari, M. et al. The SAURON project—X. The orbital anisotropy of elliptical and lenticular galaxies: revisiting the $(V/\sigma, \epsilon)$ diagram with integral-field stellar kinematics. *Mon. Not. R. Astron. Soc.* **379**, 418–444 (2007).

89. Wang, B., Cappellari, M. & Peng, Y. Physical explanation for the galaxy distribution on the (λ_R, ϵ) and $(V/\sigma, \epsilon)$ diagrams or for the limit on orbital anisotropy. *Mon. Not. R. Astron. Soc.* **500**, L27–L31 (2021).

90. Martin, D. C. et al. The Galaxy Evolution Explorer: a space ultraviolet survey mission. *Astrophys. J. Lett.* **619**, L1–L6 (2005).

91. Noll, S. et al. Analysis of galaxy spectral energy distributions from far-UV to far-IR with CIGALE: studying a SINGS test sample. *Astron. Astrophys.* **507**, 1793–1813 (2009).

92. Boquien, M. et al. CIGALE: a Python code investigating galaxy emission. *Astron. Astrophys.* **622**, A103 (2019).

93. Wright, E. L. et al. The Wide-field Infrared Survey Explorer (WISE): mission description and initial on-orbit performance. *Astron. J.* **140**, 1868–1881 (2010).

94. Chabrier, G. Galactic stellar and substellar initial mass function. *Publ. Astron. Soc. Pac.* **115**, 763–795 (2003).

95. Cappellari, M. et al. The ATLAS^{3D} project—XV. Benchmark for early-type galaxies scaling relations from 260 dynamical models: mass-to-light ratio, dark matter, fundamental plane and mass plane. *Mon. Not. R. Astron. Soc.* **432**, 1709–1741 (2013).

96. Sánchez, S. F. et al. Pipe3D, a pipeline to analyze integral field spectroscopy data: I. New fitting philosophy of FIT3D. *Rev. Mexicana Astron. Astrofis.* **52**, 21–53 (2016).

97. Salpeter, E. E. The luminosity function and stellar evolution. *Astrophys. J.* **121**, 161 (1955).

Acknowledgements

Author contributions

B.W., Y.P. and M.C. all contributed extensively and significantly to the work presented in this paper, including the analyses, presentation and interpretation of the data. B.W. finished writing the first version of paper, after which all authors worked closely on revisions.

Competing interests

The authors declare no competing interests.

Additional information

Extended data is available for this paper at https://doi.org/10.1038/s41550-024-02376-8.

Supplementary information The online version contains supplementary material available at https://doi.org/10.1038/s41550-024-02376-8.

Correspondence and requests for materials should be addressed to Bitao Wang or Yingjie Peng.

Peer review information *Nature Astronomy* thanks Matthew Bershady, Nicholas Boardman and the other, anonymous, reviewer(s) for their contribution to the peer review of this work.

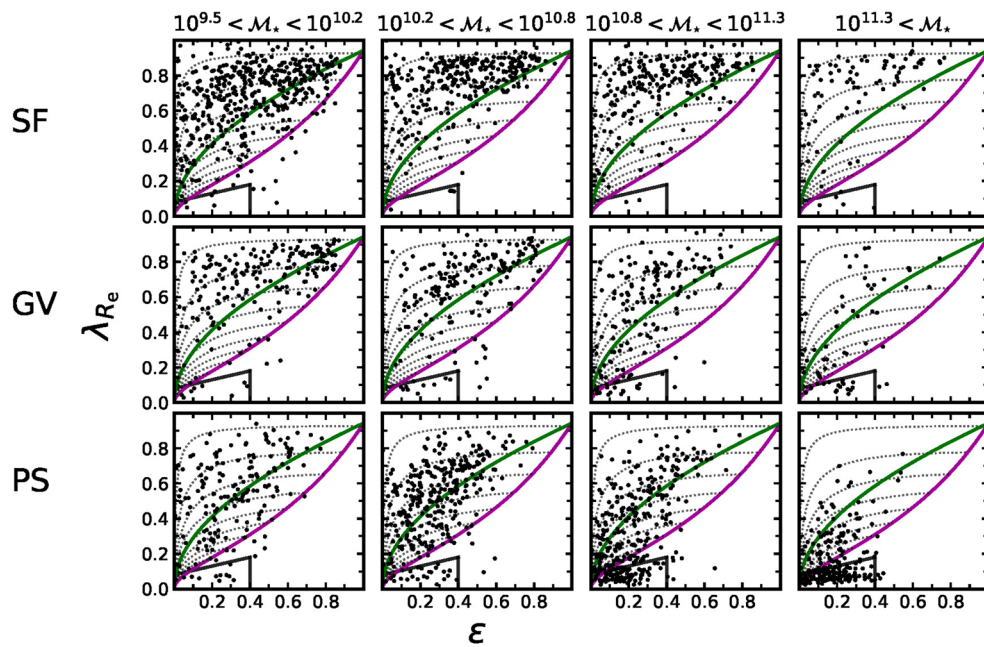**Reprints and permissions information** is available at www.nature.com/reprints.

Extended Data Fig. 1 | Galaxy distributions on the λ_{R_e} versus ε diagram. The stellar mass and star formation bins are the same as in Fig. 2. Black dots represent the observed MaNGA galaxies. The solid magenta line shows the locus of edge-on oblate rotators of varying intrinsic ellipticity ε_{intr}, at the velocity anisotropy $\delta = 0.7\varepsilon_{intr}$, predicted by the tensor virial theorem. Starting from the magenta line, the black dotted lines show how the observed λ_{R_e} and ε drop with decreasing inclination. While the magenta line assumes maximally anisotropic velocity dispersion based on empirical and theoretical evidence (refs. 88,89), the green line shows the locus of isotropic velocity dispersion. The classic slow rotators are defined by the trapezoidal area at the lower left.
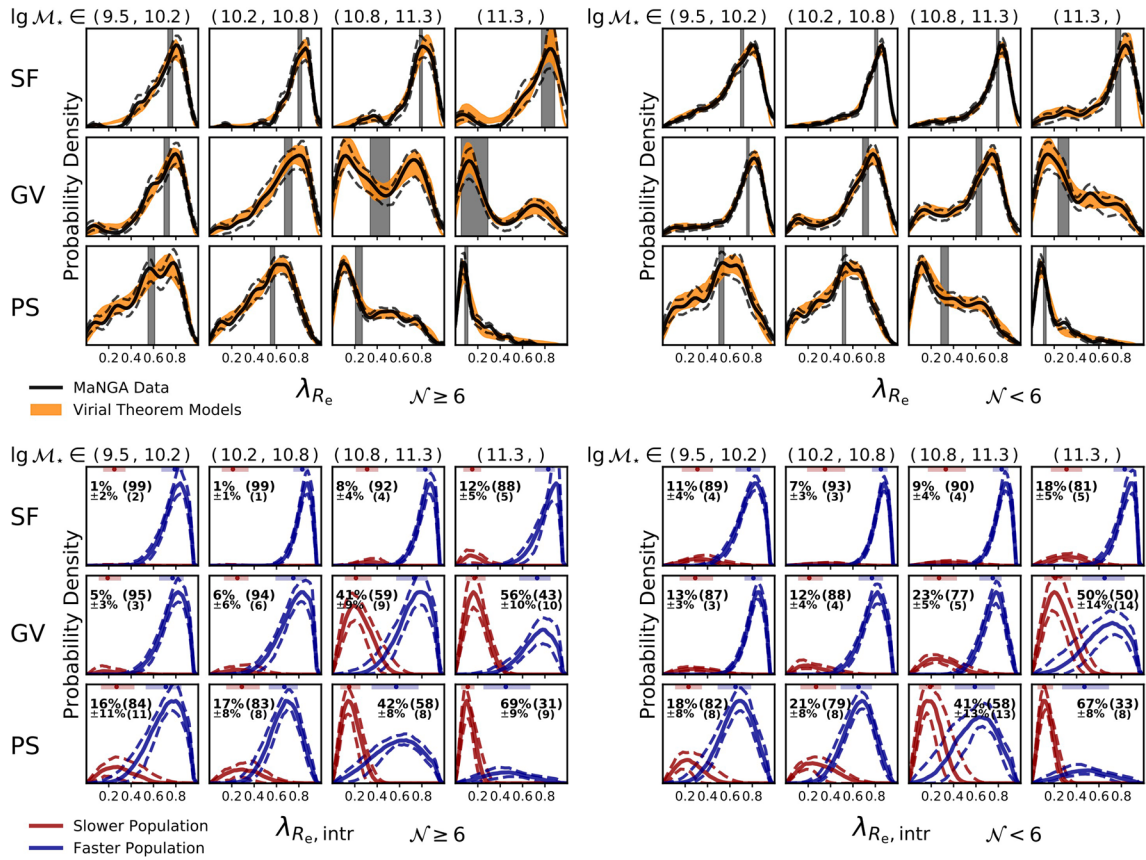
Extended Data Fig. 2 | The λ_{R_e} and $\lambda_{R_e,intr}$ distributions of galaxies in different environments. The same as in Fig. 2 but now the galaxies are divided into those in large galaxy groups (left-hand half) and in small groups (right-hand half) based on the dedicated group catalogue (ref. 29) for MaNGA galaxies.
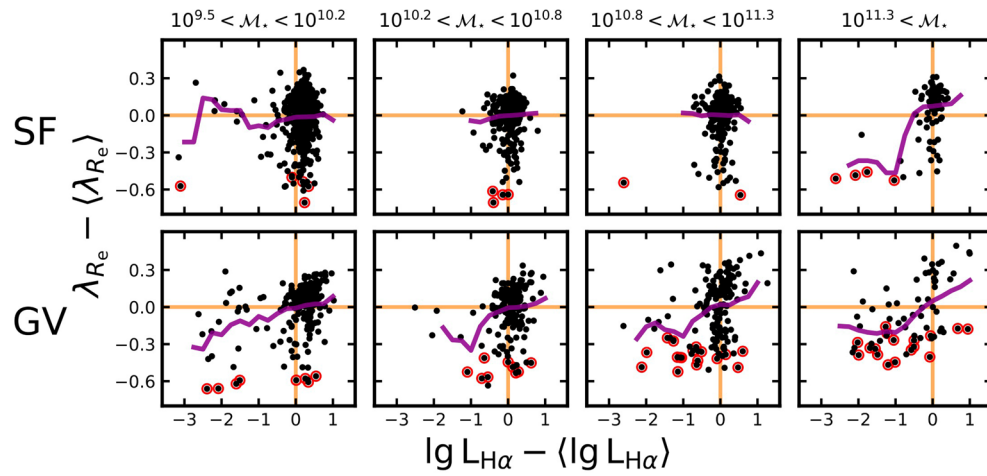
Extended Data Fig. 3 | The correlation between stellar angular momentum and recent star formation history. The dimension-reduced version of Fig. 3, without LOESS smoothing. Each panel directly shows $\lambda_{R_e} - \langle \lambda_{R_e} \rangle$ versus a measure of recent SFH, $\lg L_{H\alpha} - \langle \lg L_{H\alpha} \rangle$. $\langle \lg L_{H\alpha} \rangle$ is the expected Hα luminosity given the SED SFR, according to the quadratic fit to all galaxies shown by the black dashed curve in the upper rightmost panel of Fig. 3. The magenta lines are running average to indicate the trend. Red circles mark the classic slow rotator galaxies defined by equation 19 of ref. 11.